Influence of Cobalt Doping on the Thermoelectric Properties of the Magnéli Phase W_<18>O_<49>

Mostafa M. ELKADY
Department of Applied Science for Electronics and Materials, Interdisciplinary Graduate School of Engineering Sciences, Kyushu University

OHTAKI, Michitaka
Department of Applied Science for Electronics and Materials, Interdisciplinary Graduate School of Engineering Sciences, Kyushu University

SUEKUNI, Koichiro
Department of Applied Science for Electronics and Materials, Interdisciplinary Graduate School of Engineering Sciences, Kyushu University

https://doi.org/10.5109/7323399

出版情報：Proceedings of International Exchange and Innovation Conference on Engineering & Sciences (IEICES). 10, pp.1129-1134, 2024-10-17. International Exchange and Innovation Conference on Engineering & Sciences
バージョン：

Influence of Cobalt Doping on the Thermoelectric Properties of the Magnéli Phase $W_{18}O_{49}$

Mostafa M. ELKADY [1], Michitaka OHTAKI [1,2], Koichiro SUEKUNI [1,2]

[1] Department of Applied Science for Electronics and Materials, Interdisciplinary Graduate School of Engineering Sciences, Kyushu University, 6-1 Kasugakouen, Kasuga, Fukuoka, 816-8580, Japan

[2] Transdisciplinary Research and Education Center for Green Technologies, Kyushu University, 6-1 Kasugakouen, Kasuga, Fukuoka, 816-8580, Japan

Corresponding email: mostafa.kadi22@gmail.com

Abstract: *The Magnéli phase W18O49 exhibits promising thermoelectric properties owing to its high electrical conductivity and low thermal conductivity, despite its low Seebeck coefficient. In this study, (W1-xCox)18O49 ($0 \leq x \leq 0.05$) was synthesized via a solid-state reaction, followed by spark plasma sintering, to investigate the effect of cobalt dopants on the thermoelectric properties of W18O49. The XRD analysis indicated the formation of W18O49-based phase and the secondary phase CoWO4. The cobalt substitution decreased both the electrical and thermal conductivities while slightly increased the Seebeck coefficient. These reduction in the thermal conductivity led to enhanced thermoelectric performance. The dimensionless figure of merit (ZT) reached to 0.022 at 1073 K for x = 0.05.*

Keywords: Tungsten suboxide, Thermoelectric, Spark plasma sintering

1. INTRODUCTION

Growing sense of urgency about global climate change has driven the exploration of novel energy sources alternative to fossil fuels. Thermoelectric (TE) energy conversion has attracted attention due to its ability to directly convert waste heat into electricity (without emitting greenhouse gasses), making it a promising option for enhancing energy conversion efficiency and reducing reliance on fossil fuels [1]. The thermal-to-electrical energy conversion is based on the Seebeck effect: an electromotive force (voltage) appears when a solid (TE material) is subjected to a temperature gradient. The magnitude of the voltage, ΔV, induced between both ends of the solid per unit temperature difference is referred to as the Seebeck coefficient, $S = -\Delta V/\Delta T$, where ΔT is the temperature difference. For efficient energy conversion, TE materials should have large S as well as high electrical conductivity, σ, and low thermal conductivity, κ. The latter two characteristics are required for decreasing internal resistance of a generator and for maintaining a sufficient ΔT between the hot side and cold side of a TE material, respectively [2]. The performance of a TE material can be determined by combining these parameters (S, σ, κ) as $ZT = S^2\sigma T\kappa^{-1}$, where Z is referred to as the figure of merit and T is the absolute temperature. In addition to the high ZT, TE materials should have low-cost and environmentally-benign characteristics of the constituent elements and good stability at high temperatures. [3] The best example is oxides, *e.g.*, ZnO [4], $Ca_3Co_4O_9$ [5], $CaMnO_3$ [6], $SrTiO_3$ [7], A_xCoO_2 (A = Na, Ca, Sr, Ba) [8], Ba_3BO (B = Si, Ge) [9].

$W_{18}O_{49}$, a sub-stoichiometric tungsten oxide, has garnered interest because of its potential TE properties. This compound is characterized by the unique crystal structure and n-type metallic properties. The crystal structure of $W_{18}O_{49}$ is composed of distorted WO_6 octahedra, which are linked by sharing corners. The W ion is expected to be in the W^{+6} and W^{+5} valence states [10, 11]. One strategy for boosting the TE performance is to decrease the electron carrier concentration to increase the absolute value of S and decrease the electronic thermal conductivity, κ_{ele}. An example is the substitution of Ti^{4+} for W^{5+}/W^{6+}, *i.e.*, $(W_{1-x}Ti_x)_{18}O_{49}$, which lead to the enhancement of ZT from 0.05 for $x = 0$ to 0.50 for $x = 0.2$ at 1073 K [12]. Although other transition metals, *e.g.*, Fe, Co, Ni, Mo, Ir, have been also selected as doping/substitution elements (for exploring nano-structured functional materials [13-16]), the TE properties of $(W_{1-x}T_x)_{18}O_{49}$ have been scarcely investigated so far. In this study, our efforts have been devoted to synthesizing the Co-doped bulk samples and to examine effects of the doping on the TE properties of $W_{18}O_{49}$.

2. EXPERIMENTAL DETAILS

Samples of $(W_{1-x}Co_x)_{18}O_{49}$ ($x = 0$, 0.03, 0.05) were synthesized via the direct reaction of metal oxides. WO_3 (Kishida Chemical, 99.9%), WO_2 (FUJIFILM Wako Chemicals, 99.9%) and CoO (FUJIFILM Wako Chemicals, 99.9%) were weighed according to the target metal/oxygen compositions and mixed in a zirconia vial using a planetary ball mill (pulverisette 6, Fritsch) at a disc rotation speed of 300 rpm for 1 h. The mixture was

then molded into pellet by applying a uniaxial pressure of 100 MPa, sealed in an evacuated quartz ampoule, and heated to 1073 K. The pellet was maintained at this temperature for 24 h, and then cooled to room temperature. The heating/cooling rate was set at approximately 373 K h^{-1}. After the initial heating cycle, the sample was thoroughly ground, pelletized again under a uniaxial pressure of 100 MPa, and then annealed at 1073 K for 24 h in an evacuated quartz ampoule to improve homogeneity. Subsequently, the pellet was reground, and the obtained powders were loaded into a graphite die with an inner diameter of 10 mm. Graphite foils were placed between the die/punch and powder. The die was placed in a spark plasma sintering (SPS) furnace (PLASMAN CSP-I-03121, S. S. Alloy). The furnace chamber was evacuated to a pressure of ≤ 10 Pa, and the sample was heated to 1423 K at a rate of 100 K min−1 and kept at this temperature for 15 min under a uniaxial pressure of 50 MPa. After released from the pressure, the sample was cooled to room temperature at 20 K min^{-1}. The pellet was taken out from the die, the carbon foil adhering to the sample surface was peeled off, and the surface was polished using an SiC abrasive paper to remove any possible carbon contamination.

The crystal structure of sample was analyzed by powder X-ray diffraction (PXRD). The data were collected in the 2θ range of 5°–90° with a step size of 0.01° using an X-ray diffractometer (MiniFlex600, Rigaku) with a CuKα radiation source operating at 40 kV and 15 mA. Morphology of the bulk sample and elemental compositions were investigated by scanning electron microscopy (SEM) and energy dispersive X-ray spectroscopy (EDS), respectively, using a microscope (JCM-6000Plus NeoScope, JEOL). The σ and S values were measured on a rectangular bar-shaped sample in a TE properties measurement system (RZ2001i, Ozawa Science) at temperatures between 344 K and 1046 K under the Ar atmosphere. The thermal diffusivity, α, and the specific heat C_p, were measured using a laser flash measurement system (LFA-502, Kyoto Electronics Manufacturing) at temperatures between 300 K and 1073 K under dynamic vacuum. The data were used to calculate $\kappa = \alpha C_p \rho$, where ρ is the bulk density of the sample estimated using its mass and dimension.

3. RESULTS AND DISCUSSION

The PXRD patterns for $(W_{1-x}Co_x)_{18}O_{49}$ (x = 0, 0.03, 0.05) are shown in Fig. 1. For the sample of x = 0, all peaks were indexed to the crystal structure of $W_{18}O_{49}$, and their relative intensities are in good agreement with those of a calculated pattern of $W_{18}O_{49}$ (ICSD card: 202488). The lattice parameters and angle obtained from the Rietveld analysis were a = 18.326 Å, b = 3.783 Å, c = 14.037 Å, and β = 115.204° ($\alpha = \gamma$ = 90°), respectively, which were consistent with the parameters previously reported [10]. The PXRD patterns for the samples of x = 0.03 and x = 0.05 showed small peaks at 2θ =19.0°, 24.6°, 31.4°, 41.3°, and 44.3°, which could be indexed to the structure of $CoWO_4$ (ICSD card: 15851). For the Co-substituted samples, the lattice parameters slightly increased to a = 18.336 Å, b = 3.785 Å, c = 14.042 Å for x = 0.05.

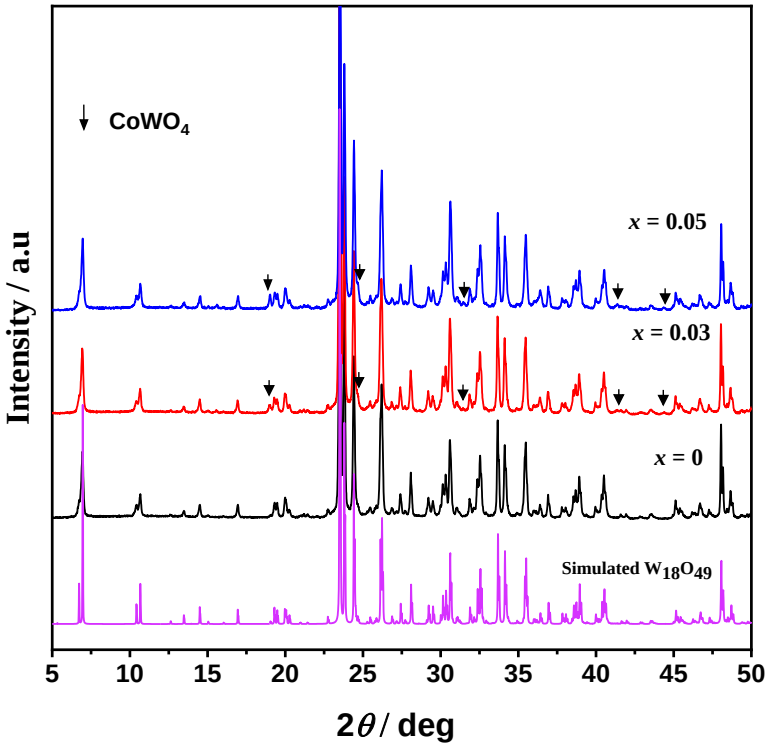

Fig. 1: Powder X-ray diffraction patterns for the samples of $(W_{1-x}Co_x)_{18}O_{49}$ (x = 0, 0.03, 0.05).

The SEM images for fracture surfaces of the samples showed closely packed grains, as depicted in Fig. 2. Indeed, the relative density of the sample of x = 0 calculated by dividing ρ by crystal density was as high as 93.8%. With increasing the Co content, the value of ρ increased, which can be attributed to the formation of the

secondary phase, $CoWO_4$. The grain size of 1–5 μm was comparable among the samples of x = 0, 0.03, and 0.05.

Fig. 3 shows backscattered electron images for polished surfaces. For the sample of x = 0, the region with bright contrast occupied most of the area, which corresponds to $W_{18}O_{49}$ according to the PXRD result. The elemental mapping proved the homogeneous distribution of elements. The Co-substituted samples were composed of two phases with bright and dark contrast. The ratio of Co to W obtained from EDS in the main phase was ~1–2%, which was smaller than the ratio (3–5%) in the nominal compositions. The low substitution level should come from the formation of $CoWO_4$. Indeed, the "Co-rich" secondary phase was observed in the elemental mapping images (Fig. 3). The amount of the secondary phase increased from x = 0.03 to x = 0.05.

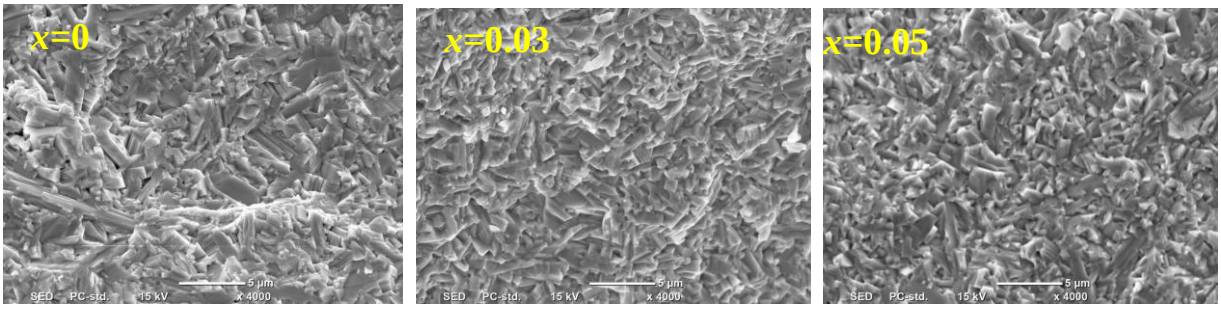

Fig. 2: Scanning electron microprobe images for fractured surfaces of the samples of $(W_{1-x}Co_x)_{18}O_{49}$ (x = 0, 0.03, 0.05).

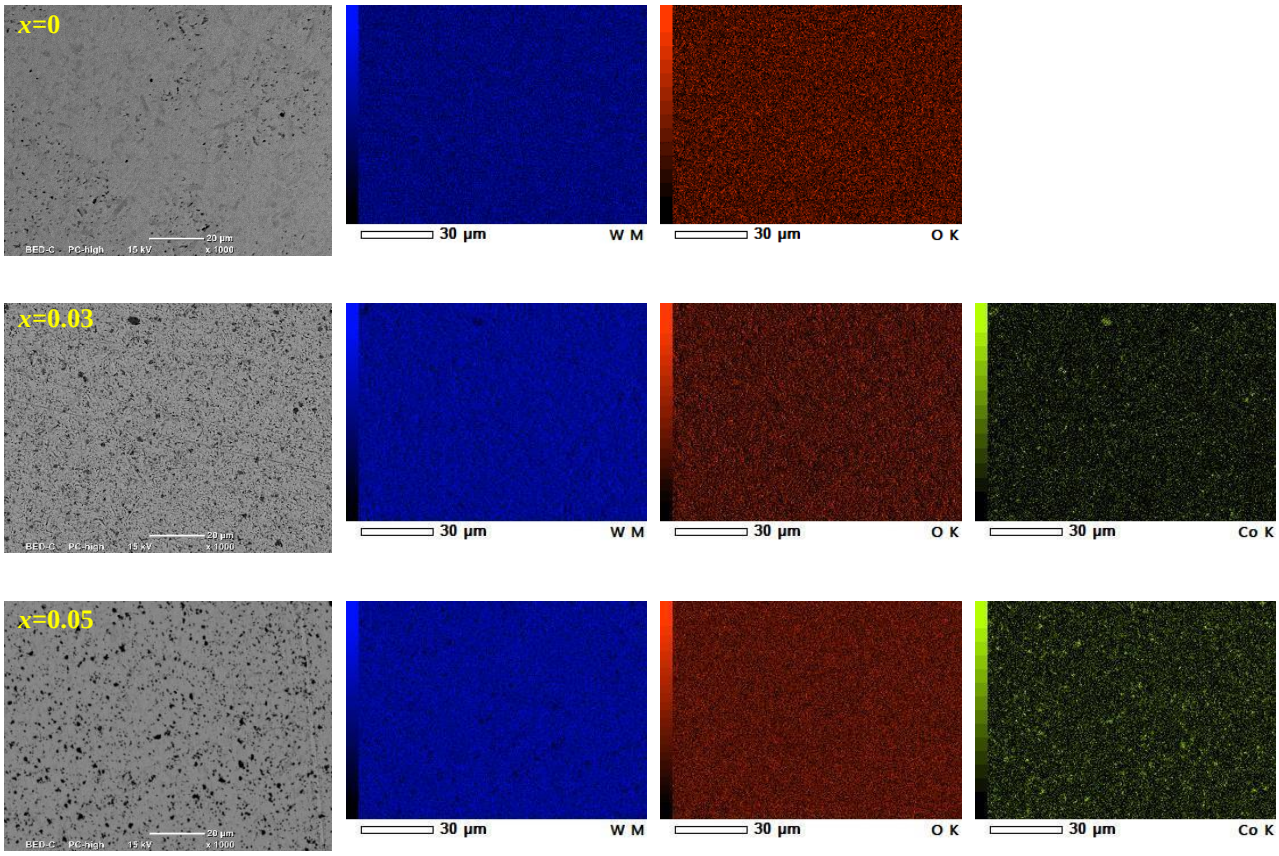

Fig. 3: Backscattered electron images and elemental mapping results for the samples of $(W_{1-x}Co_x)_{18}O_{49}$ (x = 0, 0.03, 0.05).

The temperature dependence of σ, S, and the power factor, σS^2, are shown in Fig. 4 (a-c). The σ values for the undoped sample decreased with increasing temperature from 6.41×10^3 S cm^{-1} at 300 K to 1.83×10^3 S cm^{-1} at 1073 K (Fig. 4(a)), which is consistent with the metallic behavior reported earlier [17]. When the Co concentration increased to $x = 0.03$ and 0.05, the σ values decreased slightly in the whole temperature range (Fig. 4(a)). At 300 K, σ for $x = 0.03$ and 0.05 were 6.12×10^3 and 5.15×10^3 S cm^{-1}, respectively. The dominant charge carriers in $(W_{1-x}Co_x)_{18}O_{49}$ are electrons as proven by the negative sign of S (Fig. 4(b)). With increasing Co content x, the absolute value of S at 300 K increased from 16 μVK^{-1} ($x = 0$) to 20 μVK^{-1} ($x = 0.05$), and this tendency was kept up to 1073K. The decrease in σ and the increase of the absolute value of S can be attributed to a decrease in the carrier concentration. The presence of $CoWO_4$, which exhibits semiconducting properties ($\sigma = 10^{-8}$ to 10^{-3} Ω^{-1}cm^{-1} at 750 K) [18, 19], may contribute the variations of electronic properties. As a result of the Co substitution, the value of σS^2 was remained unchanged below 700 K, while decreased from 0.25 mW K^{-2}m^{-1} ($x = 0$) to 0.17 mW K^{-2}m^{-1} ($x = 0.03$, 0.05) at 1073 K (Fig. 4(c)).

The temperature dependence of σ and S exhibited a good reproducibility over heating and cooling process for the samples of $x = 0$, 0.03. On the other hand, the sample of $x = 0.05$ showed a hysteresis in σ and S. Specifically, the σ value decreased and the absolute value of S increased after the heating. The color of the sample surface was changed from black (before heating) to silver (after cooling, Fig. 5a) during the measurement. The XRD data for the silver surface demonstrated that the surface region was mainly composed of $CoWO_4$, WO_3 and Co_3W (Fig. 5c). After scraping off the surface using a SiC abrasive paper, a black surface appeared (Fig. 5b). The XRD data for this surface shown in Fig. 5b agreed with that for the PXRD data described above (Fig. 1). Therefore, we can conclude that the decomposition of the sample occurred near the surface.

The temperature dependence of κ is shown in Fig. 6a. For the sample of $x = 0$, the κ value was 13.5 W K^{-1} m^{-1} at 300 K and decreased to 9.8 W K^{-1} m^{-1} at 1073 K. The sample of $x = 0.03$ exhibited κ comparable to that of the non-substituted system, whereas a slight decrease was seen in κ for the sample of $x = 0.05$. The lowest κ value of 7.9 W K^{-1} m^{-1} was observed for the sample of $x = 0.05$ at 1073 K. The lattice thermal conductivity, κ_{lat}, was estimated by subtracting κ_{ele} from κ. Here, κ_{ele} was calculated according to the Wiedemann-Franz law $\kappa_{ele} = LT\sigma$, where L is the Lorenz number for degenerated electron system 2.44×10^{-8} W Ω K^{-2} [21, 22]. The value of κ_{ele} was 3.9–5.1 W K^{-1} m^{-1} and nearly constant over the whole temperature range for all the samples (Fig. 6b). Therefore, the reduction in κ with increasing temperature (Fig. 6a) can be attributed to the Umklapp scattering of phonons. Indeed, the κ_{lat} value for the sample of $x = 0$ was 8.57 W K^{-1} m^{-1} at 300 K and decreased to 5.2 W K^{-1} m^{-1} at 1047 K (Fig. 6c). The κ_{lat} values were comparable to that of κ_{ele} at temperatures above 600 K The κ_{lat} value was slightly increased for $x = 0.03$, while decreased for $x = 0.05$ at temperatures above 700 K. Thus, the reduction in κ for the samples of $x = 0.05$ was due to the decreases in both κ_{ele} and κ_{lat}. It was difficult to extract the effects of the substitution of Co for W and the existence of secondary phase, $CoWO_4$, on κ from the obtained data.

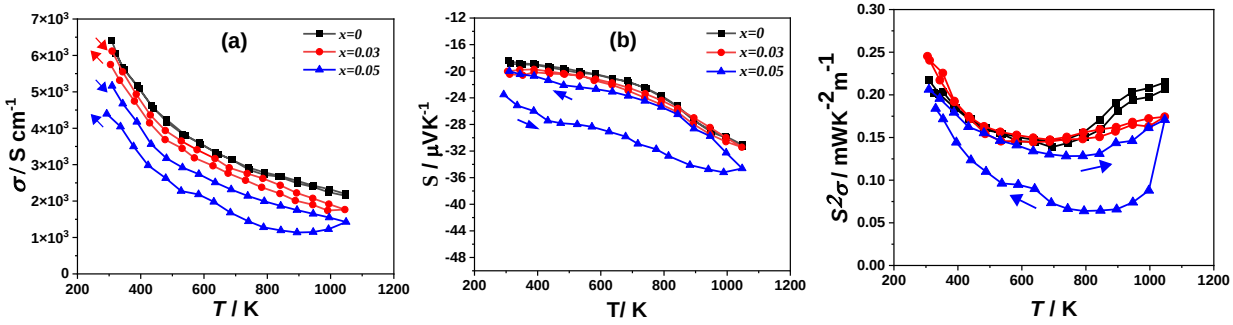

Fig. 4: (a) The electrical conductivity σ, (b) the Seebeck coefficient S, and (c) the power factor σS^2 for the samples of $(W_{1-x}Co_x)_{18}O_{49}$ ($x = 0$, 0.03, 0.05).

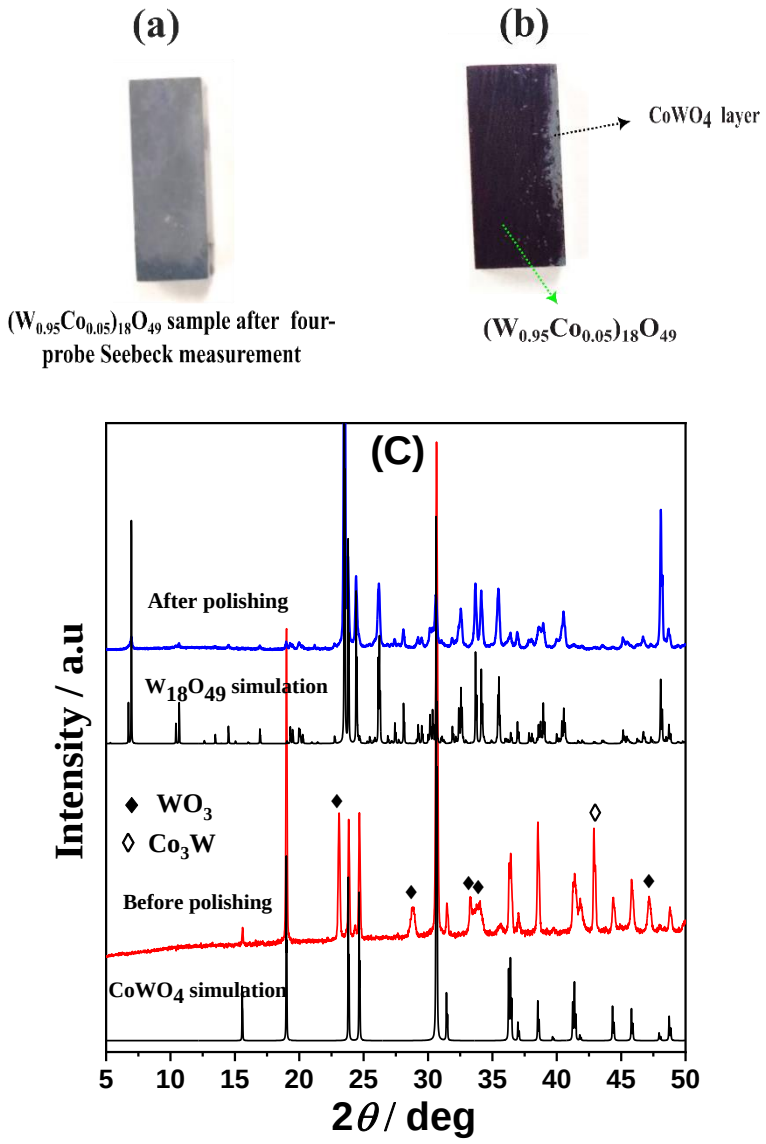

Fig. 5: Photographs of the sample of x = 0.05 after (a) the electrical properties measurement and (b) subsequent polishing; (c) X-ray diffraction patterns measured for the sample surface after the measurement and the polishing.

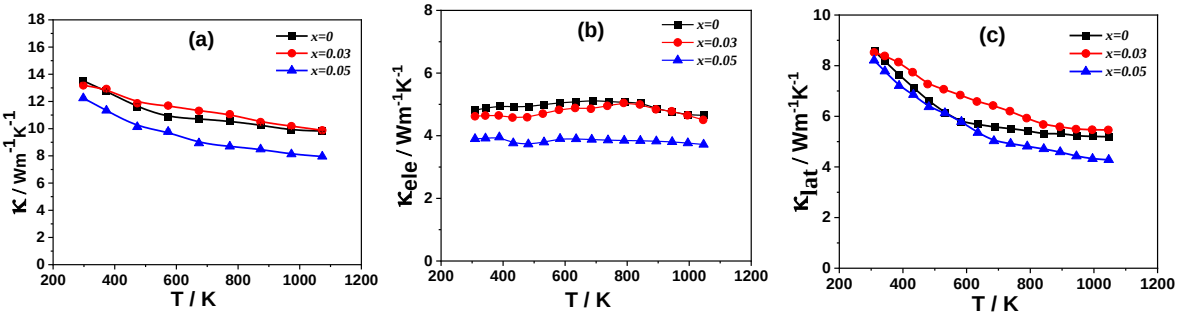

Fig. 6: (a) The thermal conductivity κ, (b) the electronic thermal conductivity κ_{ele}, (c) the lattice thermal conductivity κ_{lat} for the samples of $(W_{1-x}Co_x)_{18}O_{49}$ (x = 0, 0.03, 0.05).

The value of ZT for x = 0 was 0.006 at 300 K and increased to 0.016 at 1073 K (Fig. 7). With increasing x, ZT at 1073 K was enhanced to 0.018 and 0.022 for x = 0.03 and x = 0.05, respectively. The enhancement of ZT was due to the decreases in κ_{ele} and κ_{lat}. For boosting ZT, κ_{ele} and κ_{lat} should be further decreased. In order to do this, more effective dopants for decreasing the electron carrier concentration to decrease κ_{ele} as well as for introducing a large distortion in the crystal structure to scatter the phonons are required to be discovered.

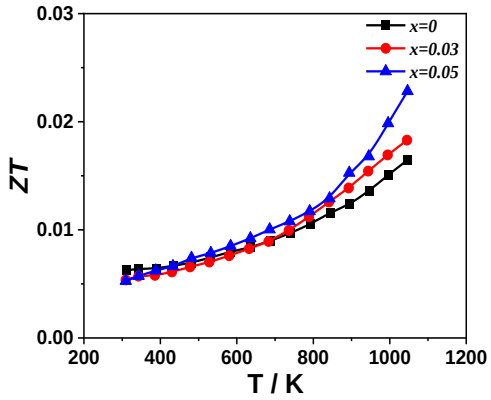

Fig. 7: Dimensionless figure of merit, ZT, for the samples of (W1−xCox)18O49 (x = 0, 0.03, 0.05).

4. CONCLUSION

We have investigated the effects of the substitution of Co for W on the TE properties for $W_{18}O_{49}$ The $(W_{1-x}Co_x)_{18}O_{49}$ ($0 \leq x \leq 0.05$) samples were synthesized through the direct reaction of metal oxides, followed by SPS. The actual composition of Co was probably smaller than the nominal composition due to the formation of the secondary phase, $CoWO_4$. The small substitution level less than 2% resulted in the limited variations in the TE properties. For the sample for x = 0.05, although σS^2 decreased compared to the non-substituted sample, the decreases in κ_{ele} and κ_{lat} gave rise to an enhancement of *ZT*.

5. References

1. d'Angelo, M., C. Galassi, and N. Lecis, *Thermoelectric Materials and Applications: A Review.* Energies, 2023. **16**(17): p. 6409.
2. Schierning, G., et al., *Concepts for medium-high to high temperature thermoelectric heat-to-electricity conversion: a review of selected materials and basic considerations of module design.* Translational Materials Research, 2015. **2**(2): p. 025001.
3. Yan, Q. and M.G. Kanatzidis, *High-performance thermoelectrics and challenges for practical devices.* Nature Materials, 2022. **21**(5): p. 503-513.
4. Sulaiman, S., et al., *Review on grain size effects on thermal conductivity in ZnO thermoelectric materials.* RSC Advances, 2022. **12**(9): p. 5428-5438.
5. Hira, U., et al., *Improved High-Temperature Thermoelectric Properties of Dual-Doped Ca3Co4O9.* ACS Omega, 2022. **7**(8): p. 6579-6590.
6. Kanas, N., et al., *Tuning the Thermoelectric Performance of CaMnO3-Based Ceramics by Controlled Exsolution and Microstructuring.* ACS Applied Energy Materials, 2022. **5**(10): p. 12396-12407.
7. Shi, X.-L., et al., *SrTiO3-based thermoelectrics: Progress and challenges.* Nano Energy, 2020. **78**: p. 105195.
8. Kanno, T., S. Yotsuhashi, and H. Adachi, *Anisotropic thermoelectric properties in layered cobaltite AxCoO2 (A=Sr and Ca) thin films.* Applied Physics Letters, 2004. **85**(5): p. 739-741.
9. He, X., et al., *Inverse-Perovskite Ba3BO (B = Si and Ge) as a High Performance Environmentally Benign Thermoelectric Material with Low Lattice Thermal Conductivity.* Advanced Science, 2024. **11**(10): p. 2307058.
10. Viswanathan, K., K. Brandt, and E. Salje, *Crystal structure and charge carrier concentration of W18O49.* Journal of Solid State Chemistry, 1981. **36**(1): p. 45-51.
11. Yan, N.-F., et al., *Recent progress of W18O49 nanowires for energy conversion and storage.* Tungsten, 2023. **5**(4): p. 371-390.
12. Tran, N.Q.M., M. Ohtaki, and K. Suekuni, *High-temperature thermoelectric performance of (W1-xTix)18O49.* Journal of the European Ceramic Society, 2022. **42**(4): p. 1486-1492.
13. Hai, G., et al., *Fe, Ni-codoped W18O49grown on nickel foam as a bifunctional electrocatalyst for boosted water splitting.* Dalton Transactions, 2021. **50**(33): p. 11604-11609.
14. Xiong, J., et al., *Electronic state tuning over Mo-doped W18O49 ultrathin nanowires with enhanced molecular oxygen activation for desulfurization.* Separation and Purification Technology, 2022. **294**.
15. Hai, G., et al., *Activation of urchin-like Ni-doped W18O49/NF by electrochemical tuning for efficient water splitting.* Journal of Energy Chemistry, 2021. **63**: p. 642-650.
16. Yan, T., et al., *IrO2 Nanoparticle-Decorated Ir-Doped W18O49 Nanowires with High Mass Specific OER Activity for Proton Exchange Membrane Electrolysis.* ACS Applied Materials and Interfaces, 2023. **15**(5): p. 6912-6922.
17. Tran, N.Q.M., M. Ohtaki, and K. Suekuni, *Rapid Synthesis of $W_{18}O_{49}$ via Reactive Spark Plasma Sintering with Controlled Anisotropic Thermoelectric Properties.* 2021.
18. Bharati, R., R. Singh, and B. Wanklyn, *On electrical transport in CoWO 4 single crystals.* Journal of Materials Science, 1981. **16**: p. 775-779.
19. Jeyakanthan, M. and U. Subramanian, *Enhanced DC conductivity and Seebeck coefficient of CoWO4/PbWO4 nanocomposites: role of interface.* Applied Physics A, 2021. **127**(7): p. 569.
20. TRAN, N.Q.M., *High Temperature Thermoelectric Properties of $W_{18}O_{49}$-based Materials*, in *Department of Applied Science for Electronics and Materials*. 2021, Kyushu University.
21. Franz, R. and G. Wiedemann, *Ueber die Wärme-Leitungsfähigkeit der Metalle.* Annalen der Physik, 1853. **165**(8): p. 497-531.
22. Lorenz, L., *Bestimmung der Wärmegrade in absolutem Maasse.* Annalen der Physik, 1872. **223**(11): p. 429-452.